Dynamic response and failure mechanisms of a laser-fabricated flexible thin film strain gauge

Ningyue Mao[1], Pablo D. Enrique[1,2], Albert I.H. Chen[2], Norman Y. Zhou[1], Peng Peng[1]*

[1] Centre of Advanced Materials Joining, Department of Mechanical and Mechatronics Engineering, University of Waterloo, 200 University Avenue West, Waterloo, Ontario, N2L 3G1, Canada

[2] Forcen Inc., 1485 Dupont Street, Suite 309, Toronto, Ontario, M6P 3S2, Canada

*Corresponding author: peng.peng@uwaterloo.ca

This is an author generated post-print of the article:

Ningyue Mao, Pablo D. Enrique, Albert IH Chen, Norman Y. Zhou, and Peng Peng. "Dynamic response and failure mechanisms of a laser-fabricated flexible thin film strain gauge." Sensors and Actuators A: Physical (2022): 113655.

The final citeable publication can be found here: https://doi.org/10.1016/j.sna.2022.113655

Abstract

Increasing demand for smart devices has spurred the development of advanced sensors with smaller and more adaptable form factors. The integration of thin film technology into sensors such as strain gauges has the potential to reduce their size and allow for the use of new manufacturing techniques. However, fabrication of reliable thin film strain gauges remains a challenge. Here, we demonstrate the manufacture of a 1025 Ω flexible thin film strain gauge using a UV laser patterning process and evaluate its dynamic tensile response. The strain gauges exhibit a sensitivity comparable to conventionally fabricated commercial alternatives, and can reliably survive 10^6 cycles up to 1750 με. Above this strain level, several failure mechanisms are identified, with unique electrical responses corresponding to physical damage observed on the strain gauges. These findings provide a guide to diagnose thin film strain gauge failures, demonstrate an unconventional fabrication technique, and show their potential for use in long-term dynamic load sensing applications.

Keywords: thin-film, laser processing, strain gauge, flexible devices, fatigue failure

---

1. Introduction

Industrial and consumer demand has driven the adoption of the Internet of Things (IoT), integrating sensors for real-time data capture in a wide range of applications. The ability to measure deformation acting on a surface is useful in applications including the monitoring of building and structure health [1], monitoring human health [2], and facilitating human-machine interactions [3]. This is often done with the use of a strain gauge, a device capable of measure the strain of a surface under force, pressure, and torque loads by converting mechanical distortion into an electrical signal. The principal sensing mechanism comes from the dimensional change that occurs when a strain is applied, which causes the electrical resistance of the sensor to change. With the use of thin film sensing layer, the size of large resistance strain gauges can be greatly reduced, and the strain gauge would have negligible mechanical stiffness [4]. Compared to traditional rigid sensors, flexible thin film strain gauges can be applied to arbitrarily curved surfaces such as human skin and robotic arms, and can measure a larger range of deformation. The most common type of flexible strain gauge consists of an insulating backing made of polyimide (PI) [5], glass-fiber-reinforced epoxy-phenolic [6], or polydimethylsiloxane (PDMS) [7], which supports a patterned strain-sensitive layer, such as Constantan (Copper-Nickel) and Karma/Evanohm (Nickel-Chromium) alloys.

Conventional strain gauges are typically fabricated using lithography-based techniques, involving slow development cycles, and harsh chemicals. This fabrication process also requires a controlled environment, and specialized training and equipment, which increases the manufacturing complexity and cost. Although lithographic patterning offers high structure resolution quality, its conformality is not good enough to be used on curved surfaces. Alternative fabrication methods that can alleviate the limitations associated with conventional lithography-based techniques are under investigation, such as advanced lithographic printing method (proximity-field nanopatterning) [8,9], additive printing [6], direct writing [10] and thin-film patterning by laser ablation [11,12]. Among these, laser patterning is a promising alternative. The complexity and cost of the process are greatly reduced since a mask or ink is not required and a short turnaround time for custom sensor designs is possible. This technique is also capable of patterning on three-dimensional surfaces with high structure resolution [13].

Sensitivity and reliability are two key characteristics of flexible strain gauges. Generally, the electrical and mechanical properties of thin films are not identical to those in the bulk form [14], such that special consideration should be taken to evaluate the properties of thin-film strain gauges. The effect of cyclic loading on the electrical response and fatigue failure of thin film strain gauges has not been well studied and is critical if they are to be widely implemented in industrial and consumer applications. In this study, NiCr-based strain gauges are fabricated by laser ablation on flexible polyimide substrates to achieve comparable gauge resistance to a commercially available strain gauge. The sensitivity and resistance response of the strain gauge towards varying dynamic tensile loads are investigated, and finally failure mechanisms are discussed.

2. Materials and Methods

2.1 Strain gauge fabrication

The thin-film strain gauges were fabricated using the steps shown in Figure 1, starting with a flexible polyimide substrate with a thickness of 75 μm. This was followed by a physical vapor deposition (PVD) step – performed by Angstrom Engineering, Canada – in which a 500 nm thick Evanohm (NiCr) layer is deposited on the substrate. The Evanohm layer is then patterned by laser ablation into the shape of a strain gauge. A UV laser system is used for patterning, with a 1 W laser, a wavelength of 355 nm, and a pulse width of 40 ns. A pulse energy of 11 µJ and an energy density of 0.23 J/mm^2 were selected for the patterning process. Since the development of strain gauges with more compact designs and smaller feature sizes are demanded, a high-precision laser system is required for microfabrication. Compared to CO_2 laser systems with longer wavelengths, which are widely used in manufacturing processes and rely on the photothermal effect, UV laser systems can reduce thermal damage to the patterned material and achieve smaller feature sizes due to a larger contribution from the photochemical effect [15,16]. The strain gauge pattern is designed to obtain a nominal 1025 Ω resistance, with curvature added to contact pads and traces to reduce the effect of sharp corners on fatigue life.

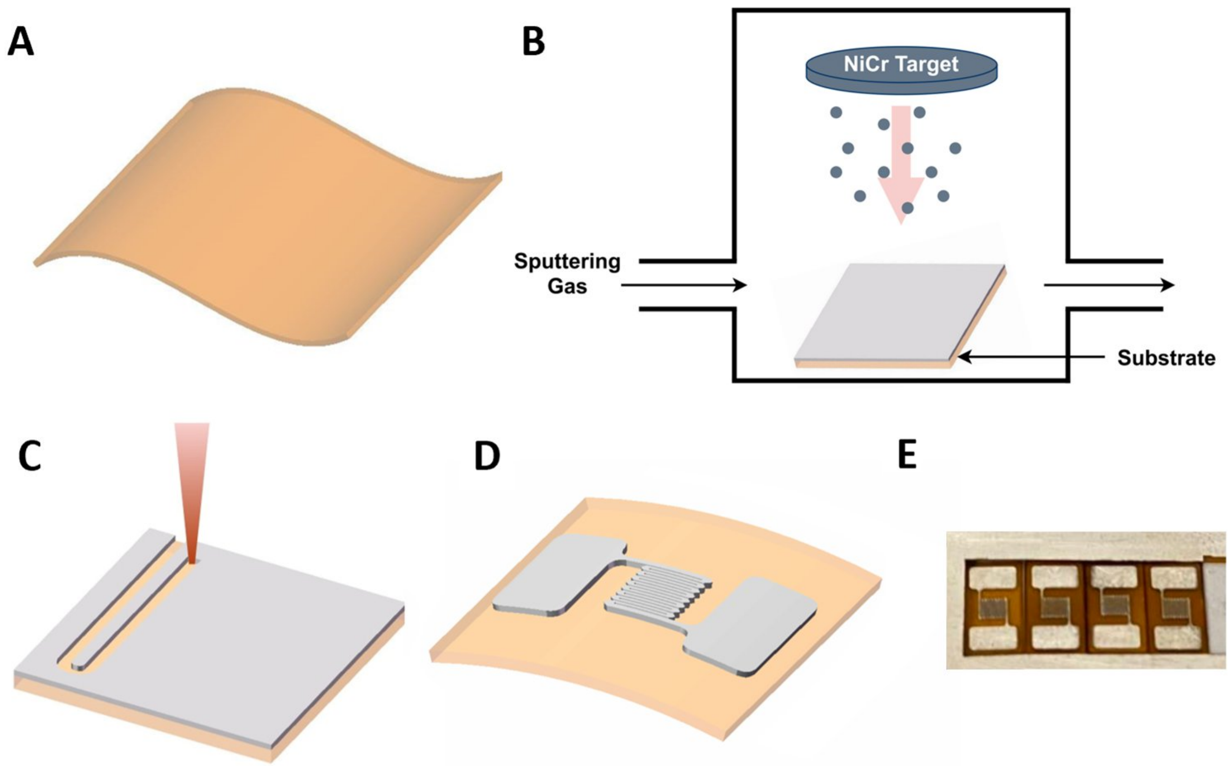

Figure 1. Schematic of the flexible thin-film strain gauge fabrication process. a) the flexible polyimide substrate; b) PVD deposition of the metallic NiCr layer; c) laser patterning of the strain gauge, d) laser fabricated thin-film strain gauge, and e) photo of fabricated strain gauge array.

2.2 Mechanical testing

To verify the sensitivity of the fabricated strain gauges, the gauge factor was measured and compared with a commercial strain gauge using a cantilever setup assembled on an Instron tensile tester (Figure 2a). A 5052 H14 tempered aluminum alloy beam with dimensions of 60 mm × 10 mm × 0.7 mm was used as the cantilever. One end of the beam is fixed on the lower grip fixture of the tensile tester and the other end is free to move. The fabricated strain gauge was attached to the top surface of the cantilever, 11 mm away from the fixed end. The upper grip of the tensile tester applies a continuous range of tensile strains on the cantilever at a constant displacement load of 1 mm/min. An Agilent 34401A digital multimeter is used to monitor and record the electrical resistance of the strain gauge as the upper grip descends. The electrical connection between the mounted strain gauge's contact pads and lead wires was soldered with a tin/lead rosin core solder wire (63% Sn, 37% Pb).

During gauge factor testing, the strain experienced at the gauge's location was calculated from the extension data returned by the tensile tester. This was done starting with Equation 1, which relates the deflection of the beam (δ) at a distance (x) from the fixed end when a known force (F) is applied at a distance (a) from the fixed end, using the beam material's modulus of elasticity (E) and moment of inertia (I). The equation can be rearranged and solved for the force at position $x = a$ using the displacement results obtained by the tensile tester as shown in Equation 2. This expression for the force can then be substituted into the equation for the bending moment at location x (Equation 3).

$$\delta = \frac{-Fx^2}{6EI}(3a - x) \tag{1}$$

$$F = \frac{-3\delta_a EI}{a^3} \tag{2}$$

$$M = -F(a - x) = \frac{3\delta_a EI}{a^3}(a - x) \tag{3}$$

The stress at location x on the top surface of the beam can be expressed as shown in Equation 4, in terms of the bending moment, half the beam thickness (c) and the moment of inertia. This expression can then be substituted into the equation for strain, as shown in Equation 5. The benefit to this approach is that it does not require knowledge of the beam's properties (E), and only requires reading of the displacement (δ_a) at position a, the position of the strain gauge on the beam (x), and half of the beam thickness.

$$\sigma = \frac{Mc}{I} = \frac{3\delta_a Ec}{a^3}(a - x) \tag{4}$$

$$\varepsilon = \frac{\sigma}{E} = \frac{3\delta_a c}{a^3}(a - x) \tag{5}$$

Long-term cyclic fatigue testing was conducted by applying dynamic tensile loading on the test beam. The test beam is prepared in a similar manner as the gauge factor test, then installed on a cyclic testing fixture (Figure 2b) with cams of different sizes to apply different deflections. The cam is driven by a DC stepper motor to apply a cyclic tensile strain at up to 4.36 Hz. As the cam rotates, the metal beam will be pushed downward and the deflection of the beam will transfer to the strain gauge, resulting in a change in its resistance. Due to the shape of the cam, one full cam rotation results in three beam bending cycles.

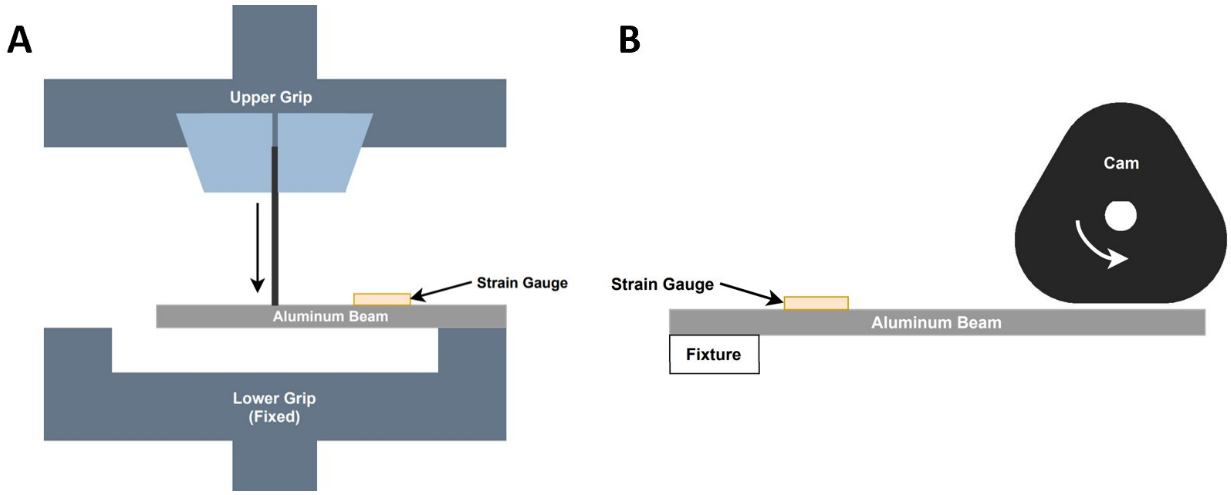

Figure 2. Schematic of experiment setup for a) gauge factor testing and b) dynamic testing.

2.3 Characterization

The microstructure and morphology of the strain gauge were characterized using scanning electron microscopy (SEM, Zeiss Leo and Zeiss Ultra Plus). The electrical properties of fabricated strain gauges were measured by a four-point probe (Keithley 4200-SCS), specifically to identify defects and causes of sensor failure by measuring and comparing the resistance of each conductive trace.

3. Results and Discussion

3.1 Strain gauge characterization

A representative sample of the final fabricated strain gauge is shown in Figure 3a, with the soldered contact pads visible in the top left and bottom right corners of the image, the winding conductive trace connecting the two contact pads visible in between, and the exposed polyimide substrate appearing dark under the SEM. A higher magnification image in Figure 3b displays a visible texture on the exposed polyimide, caused by the laser tracks used to ablate the Evanohm layer. Some spatters along the edge of the conductive trace also exist due to molten material splashing and solidifying outside of the laser ablated region. This suggests that UV laser irradiation of the NiCr thin film induces melting as expected in a nanosecond pulsed laser ablation process, and the material ablation likely occurs due to the formation of vapor and ejection of liquid droplets [17,18]. A tilted view of the conductive trace and underlying polyimide is shown in Figure 3c, showing the material buildup at the edge of the traces, and the peaks left behind by the ablation process in the exposed polyimide.

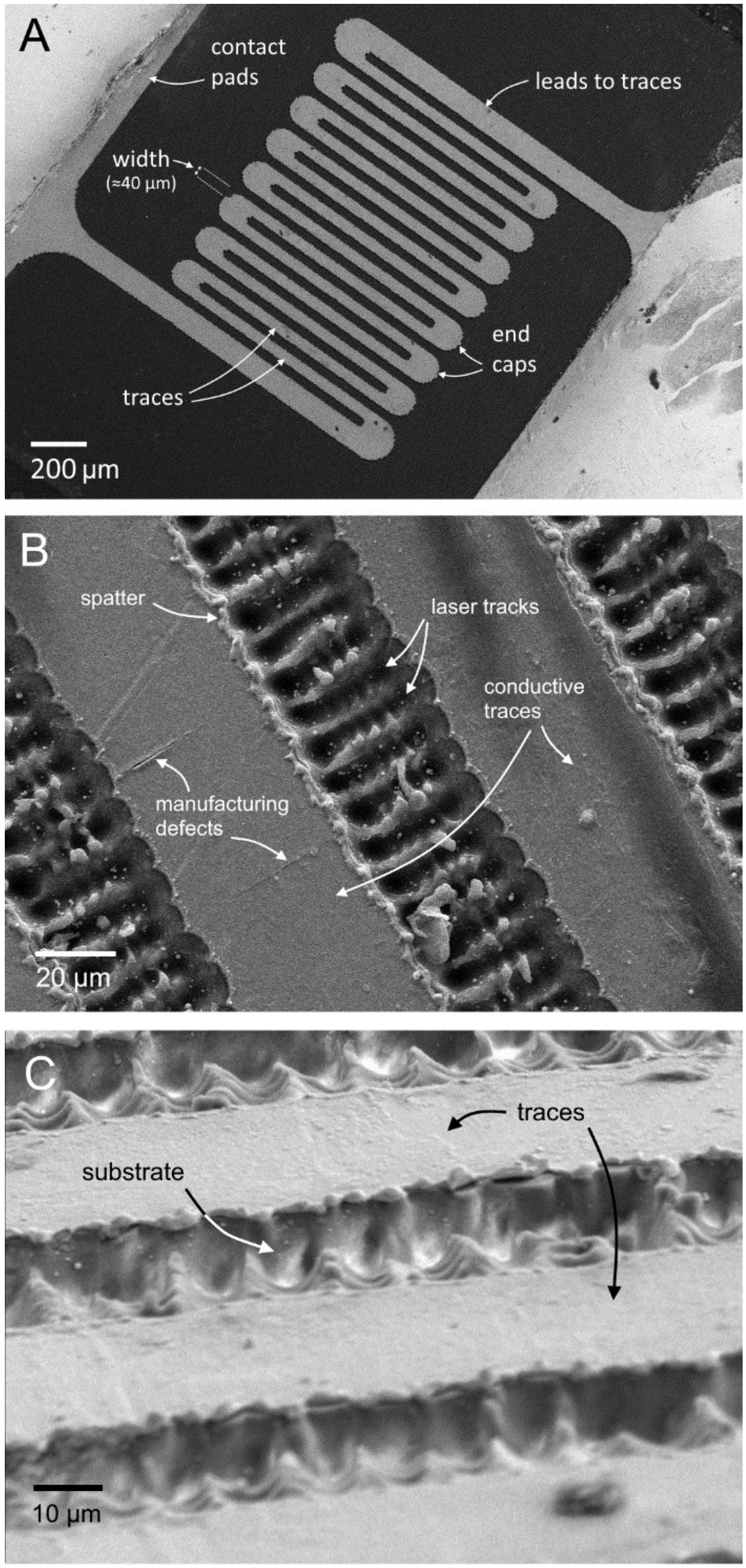

Figure 3. SEM images showing a) the strain gauge overview and terminology, b) higher magnification image of the traces, and c) a tilted view of the traces.

An average width of 40.2 µm ±3.5 µm was measured for the conductive traces in the strain gauges as labelled in Figure 3. A summation of all the lengths (L) and widths (w) in the conductive path (Table 1) that composes the strain gauge is used in Equation 6 to determine the expected resistance of the fabricated strain gauge, where ρ is the electrical resistivity of Evanohm (133 Ω·cm) and t is the Evanohm thickness (500 nm). The average measured resistance of the laser fabricated strain gauges is 1048 Ω ±53 Ω, in agreement with the calculated resistance of approximately 1025 Ω. The slight variation in the patterned strain gauge dimensions can cause slight difference in the measured resistance.

Table 1. Dimensions of conductive path as described in Figure 3a

Location	Width	Length
Leads	84.8 µm ±5.4 µm	0.31 cm
End caps	108.1 µm ±6.4 µm	0.14 cm
Traces	40.2 µm ±3.5 µm	1.35 cm

$$R = \sum_{1}^{n} \frac{\rho L_n}{t w_n} \qquad 6$$

The gauge factor, defined as the relative change in resistance ($\Delta R/R$) to the relative change in length (or strain, ε), denotes the strain gauge's sensitivity to an applied strain. This value is obtained from the slope of the linear region of the $\Delta R/R$ versus strain curves in Figure 4, with a resulting gauge factor of 2.3 ±0.2. This value is a combination of the dimensional changes and resistivity changes of the metal layer when strained, as well as the ability of the cyanoacrylate adhesive and polyimide substrate to transfer the strain from the aluminum beam to the metal layer [19]. For comparison, the gauge factor was measured for a conventionally manufactured commercial strain gauge with an Evanohm sensing layer approximately 3.5 µm thick, and was found to be 2.0 ±0.4. The two gauge factors are statistically similar and are within the expected range [20]. Although recent research has proposed supersensitive strain gauges with gauge factors larger than 5000 [21], the gauge factor is usually determined by the material composition. For Evanohm strain gauges, the gauge factor is reported to be in the range of 1.95 to 2.5 and it is constant for a film thickness of 15 nm and above [22].

Notable deviations from a linear response are observed when crack opening occurs, as can be seen in the red dotted line in Figure 4. As the crack faces separate with increasing strain, the measured resistance increases faster than would be expected due to the changing dimensions of the traces alone, a phenomenon known super-sensitivity [23]. Although some strain gauges can incorporate pre-made cracks for this purpose [21], the presence of cracks in the flexible thin film strain gauge of this study results in a non-linear response that is detrimental to the accurate correlation of resistance change to strain.

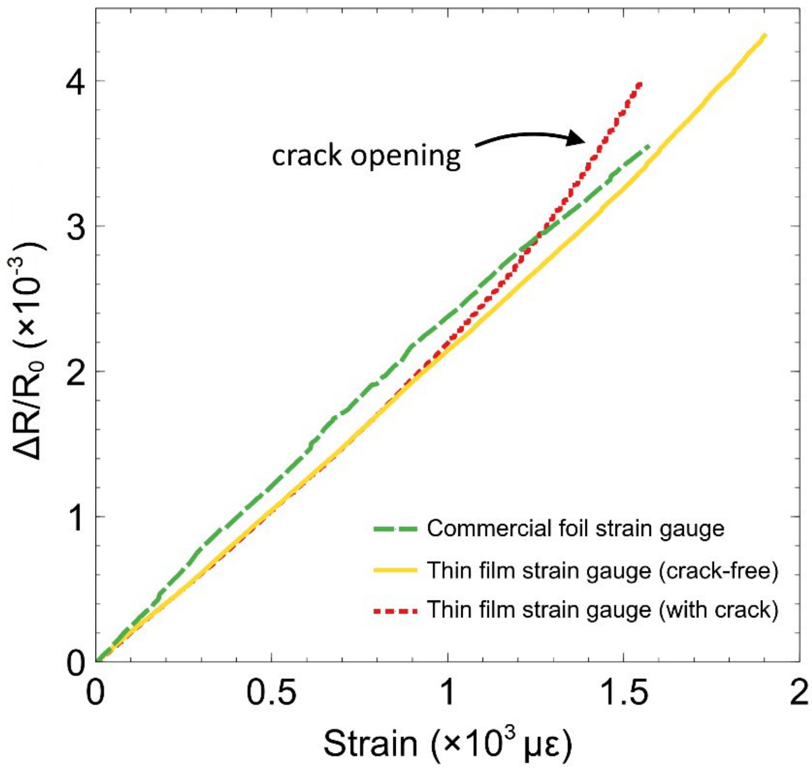

Figure 4. Example of three tensile gauge factor tests. The green (dashed) and yellow (solid) lines show the expected almost-linear response, while the red dotted line shows an apparent increase in the gauge factor caused by crack opening.

3.2 Cyclic resistance response

A total of 24 strain gauges were fatigue tested in tension at various strains, as shown in Figure 5. Failure was not observed below 1750 με while the highest strain level that resulted in a sample reaching over 10^6 cycles was 2625 με. The rated fatigue life of the commercial strain gauge with a similar sensing layer composition and substrate material is approximately 10^6 cycles at ±1800 με, or 10^6 cycles at 3240 με when only tested in tension. However, commercial strain gauges have a protective top coating, and testing conditions (testing fixture, testing frequency, adhesive, etc.) for the commercial and current thin film strain gauge are different. Above 1750 με, two failure mechanisms can be identified in the thin film strain gauges. Four samples which survived on the order of 10^3 to 10^5 cycles at elevated stain levels suffered from open circuit failures that manifested as an infinite resistance reading on the multimeter. Nine strain gauges also tested at high strain levels experienced response degradation, which includes significantly larger resistance change during cycling than expected and/or a translation of the resistance curve.

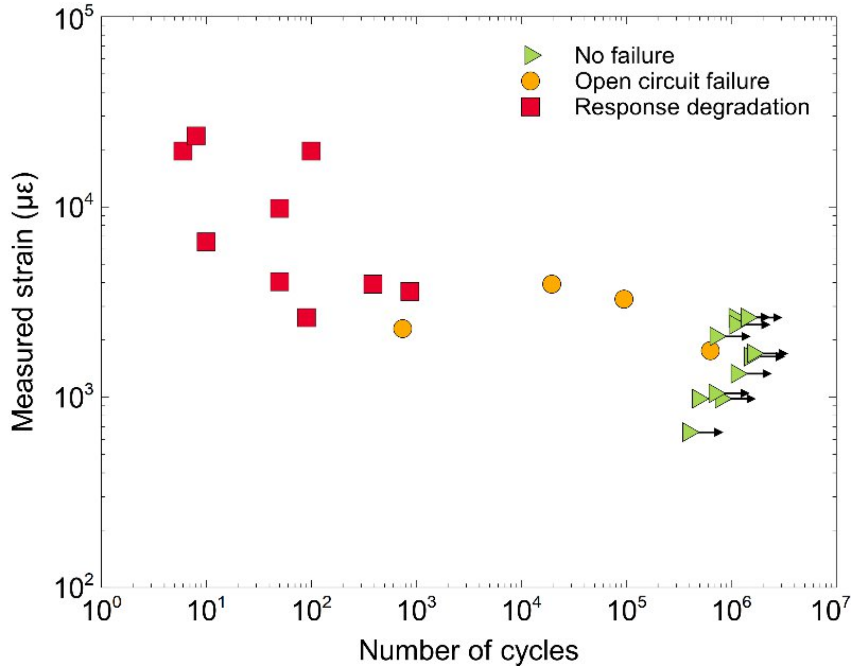

Figure 5. Results of fatigue testing of strain gauges at various strains. Tests were typically interrupted around 10^6 cycles, at which point they were considered runout samples.

Typical cyclic response is shown in Figure 6a, after the data is processed with a 5-point moving average filter to reduce noise. Strain gauges that experience runout maintain a consistent resistance change throughout the entire test, although slight variations in resistance change can be observed when looking more closely at individual cycles (Figure 6c). Since these samples are tested in tension, the resistance is at its lowest point when the beam and strain gauge are flat and at the highest point when fully bent. The amount of bending dictates the strain measured at the location on which the strain gauge is mounted to the beam. Small differences in the size of the three cam corners (Fig.2b) that induce bending result in slightly different resistance changes that repeat consistently throughout the test. When a strain gauge is in good condition – without cracks or defects as in the case of Figure 6c – the small difference in resistance response caused by the imperfect cam shape can be distinguished (labelled "cam peaks"). However, strain gauges that are damaged and are exhibiting super-sensitivity are no longer sensitive to the difference in the cam peaks (Figure 6d).

Strain gauges that exhibited an open circuit failure mode showed atypical resistance changes prior to complete failure, as shown in Figure 6b. A slight increase in the resistance change when bent was observed near 9.3×10^{-4} cycles, which is attributed to the formation of the fatigue crack and separation of the crack faces during bending. This is followed by an infinite resistance reading near 9.4694×10^{4} cycles as shown in Figure 6d. Continuing to cycle the strain gauge shows the resistance returning to the original un-strained value, explained by the crack opening fully while the strain gauge is bent and then closing fully when returned to the flat position. Further cycling shows an increase in the resistance measured when returned to the flat position, suggesting that further damage occurs and the crack faces improperly mate, until the measured resistance is infinite regardless of whether the strain gauge is bent or flat.

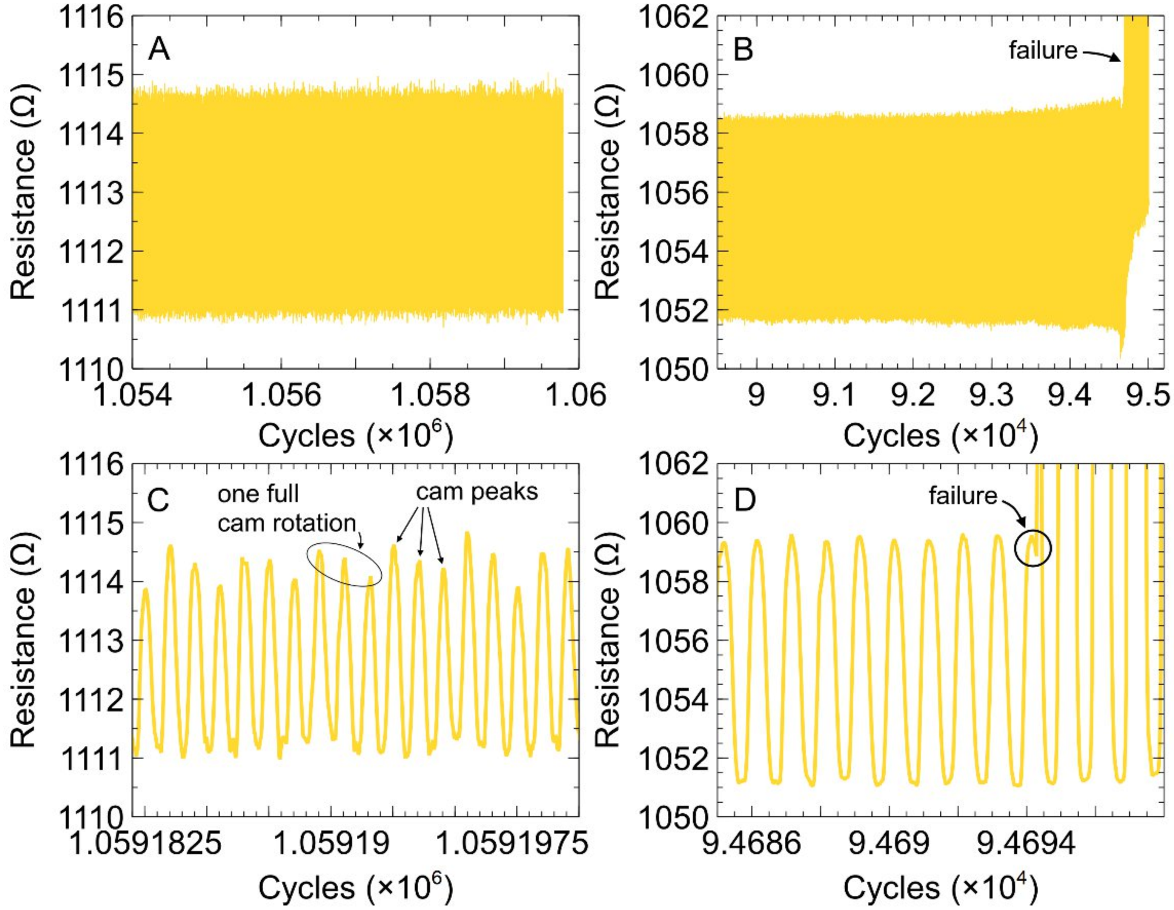

Figure 6. Cyclic response for strain gauges with a) no failure and b) open circuit failure, with higher magnification of the response curve shown in c) and d), respectively.

3.3 Failure mechanisms

Crack networks and limited material extrusion as shown in Figure 7 were observed on strain gauges with open circuit failures. Small crack networks were also visible on samples that reached runout and were considered to have not failed, although in these cases the cracks occupied a small fraction of the entire trace width. This type of failure mechanism was reported in studies of Cu and Ag films by Kraft et al [24] and Zhang et al [25], specifically identified as a transition from larger material extrusion and transgranular cracking in thicker films with larger grain sizes, to minimal extrusion and intergranular cracking in thin films with smaller grains. A decrease in grain size and decrease in film thickness are expected to increase the fatigue life. This was demonstrated by Kim et al. [26] when comparing a 200 nm Cu film to that of a 1 µm Cu film under the same bending strain conditions, showing the thicker film undergoing fatigue failure while the thinner film does not. Zhang et al [25] suggests that the small thicknesses and small grain sizes inhibit dislocation formation and movement during fatigue.

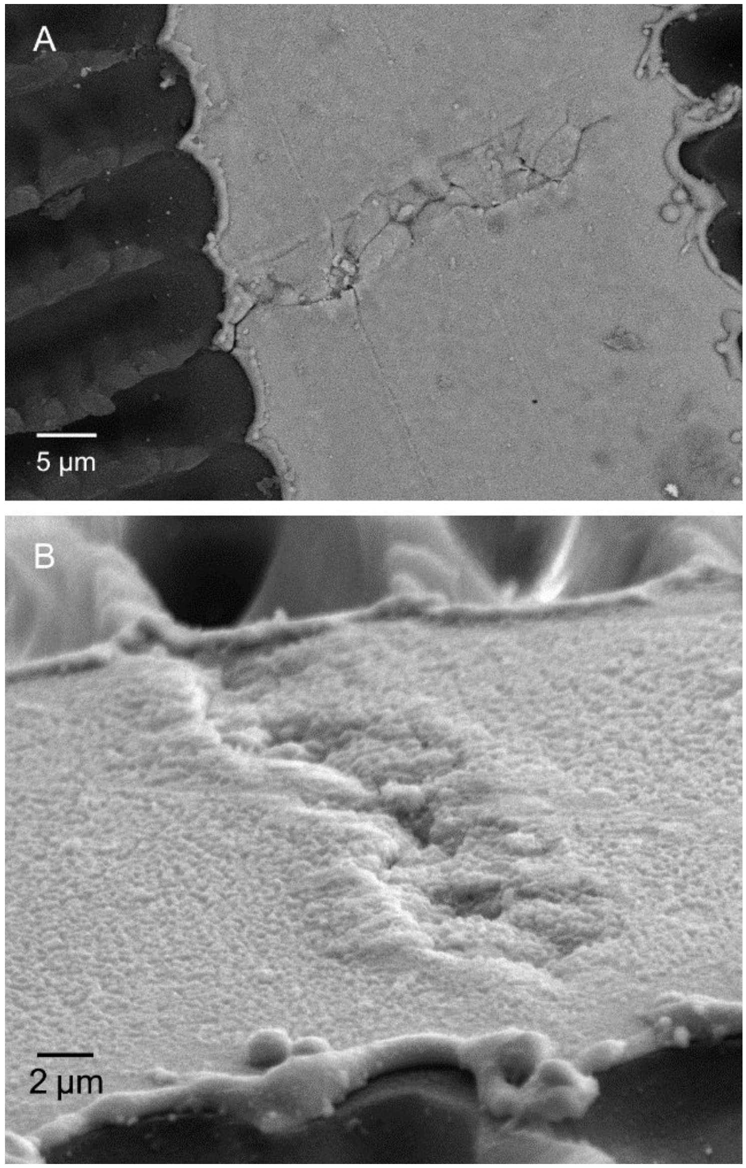

Figure 7. Crack networks viewed from a) above and b) at an angle after cyclic tensile loading.

Strain gauges that suffered from “response degradation” as labelled in Figure 5 displayed unusual cyclic responses such as increases in resistance and baseline shifts that would qualify the strain gauge as unfit for use in real-world applications. When these responses appeared during cyclic testing, the strain gauges would be considered as failed. A four-point probe was then used to evaluate the resistance of individual trace sections in both unstrained and strained conditions to identify which traces were responsible for the increased resistance or unusual response. Theoretically, the resistance of traces #2-16 should be identical while leads #1 and #17 have smaller resistance due to their larger widths (labelled as “leads to traces” in Figure 3). However, there are some small variations in resistance between traces on the same strain gauge or between different strain gauges in the as-fabricated condition as shown in Figure 8a. This can be attributed to previously identified variations in trace widths (Table 1) and the presence of small defects that can occur during laser patterning (Figure 3b). Figure 8b compares the resistance of two strain gauges that have abnormal resistance responses during long-term cyclic testing. If localized damage is occurring in the form of cracks, some traces should only experience slight increases in resistance due to bending while other damaged traces will experience larger than expected value. The first strain gauge (Sample 1) experiences larger than expected increases in resistance (based on the gauge factor and the applied deflection) on traces #2 (10 Ω), #3 (7 Ω), #5 (7 Ω), and #6 (13 Ω) in the bent condition; while the second strain gauge (Sample 2) shows significant increases in trace #2 (137 Ω), #7 (18 Ω), #8 (40 Ω), and #16 (7 Ω). Obviously, the largest contributors to the failure of Sample 2 appear in trace #2 and #8. This suggests cracks in traces with large resistance increases are opening when a strain is applied, and failure may be localized to a small number of traces while others continue to function normally.

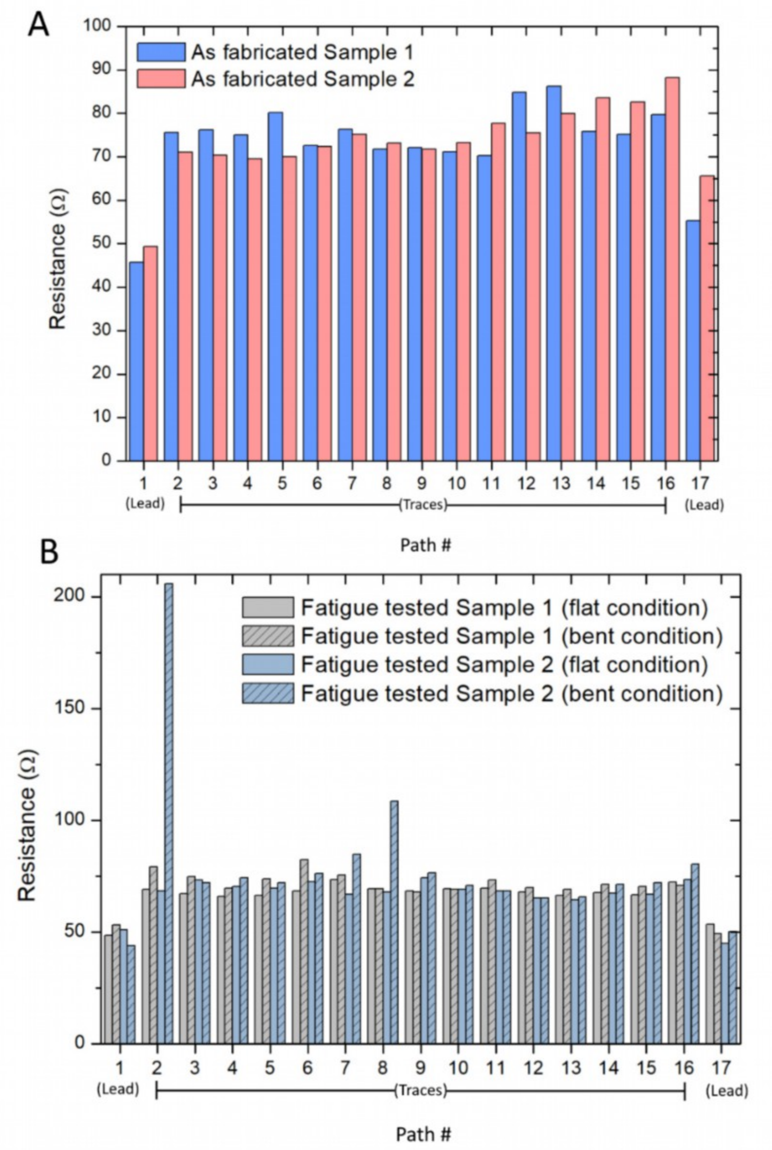

Figure 8. Comparison of individual conductive traces' resistance at flat and bent conditions for a) as-fabricated strain gauges and b) fatigue-tested strain gauges.

The first failure mode identified from resistance measurements is shown in Figure 9. This strain gauge experiences a regular cyclic response – although with larger resistance change than expected – and suddenly experiences an upward shift in resistance when returning to the flat position on each cycle as shown in Fig.9a. The larger than expected resistance change in the traces suggests that crack opening is occurring under high strain, and upward resistance shift when returning to the flat unstrained position suggests the crack faces are mating incorrectly (as proposed in Figure 9b). Figure 9c identifies delamination between the Evanohm and the polyimide at the site of cracking, which may account for the unstrained resistance shift. The crack begins to close as the beam unbends, which decreases the resistance. However, prior to reaching the fully unstrained position, the crack opens back up as the Evanohm buckles and causes a resistance increase.

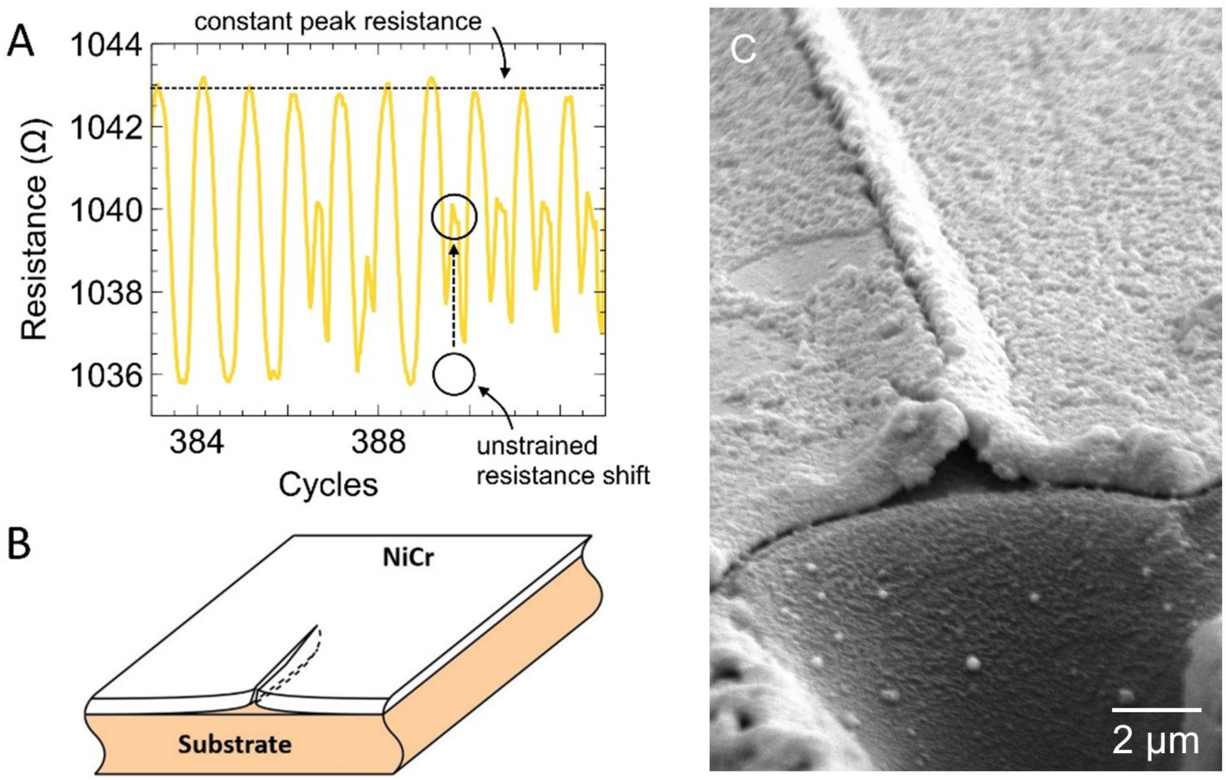

Figure 9. a) Response degradation failures showing upward shift in unstrained resistance while maintaining a constant peak resistance; b) schematic of crack and delamination after strain being released, and c) SEM image of delamination and crack in traces.

A second failure mode is shown in Figure 10, where both the peak and baseline resistance during cycling increases, but the peak resistance is a finite value and not an open circuit failure as was shown in Figure 6. Instead, the strain gauge continues to display a cyclic response, but the change in resistance is not representative of the strain experienced by the beam. The increasing peak resistance with increasing cycling suggests that crack growth is occurring, while the upwards drift in the baseline resistance indicates that the cracks do not fully close when returning to an unstrained state (Figure 10b). Figure 10c shows a SEM image of this remaining open crack when returned to the flat position. The rough crack edges suggest that an intergranular cracking mechanism may be occurring. These cracks might be initiated at the edge of traces due to the rapid cooling during laser irradiation, which can then propagate into the trace caused by residual stresses and further grow under applied stress during testing.

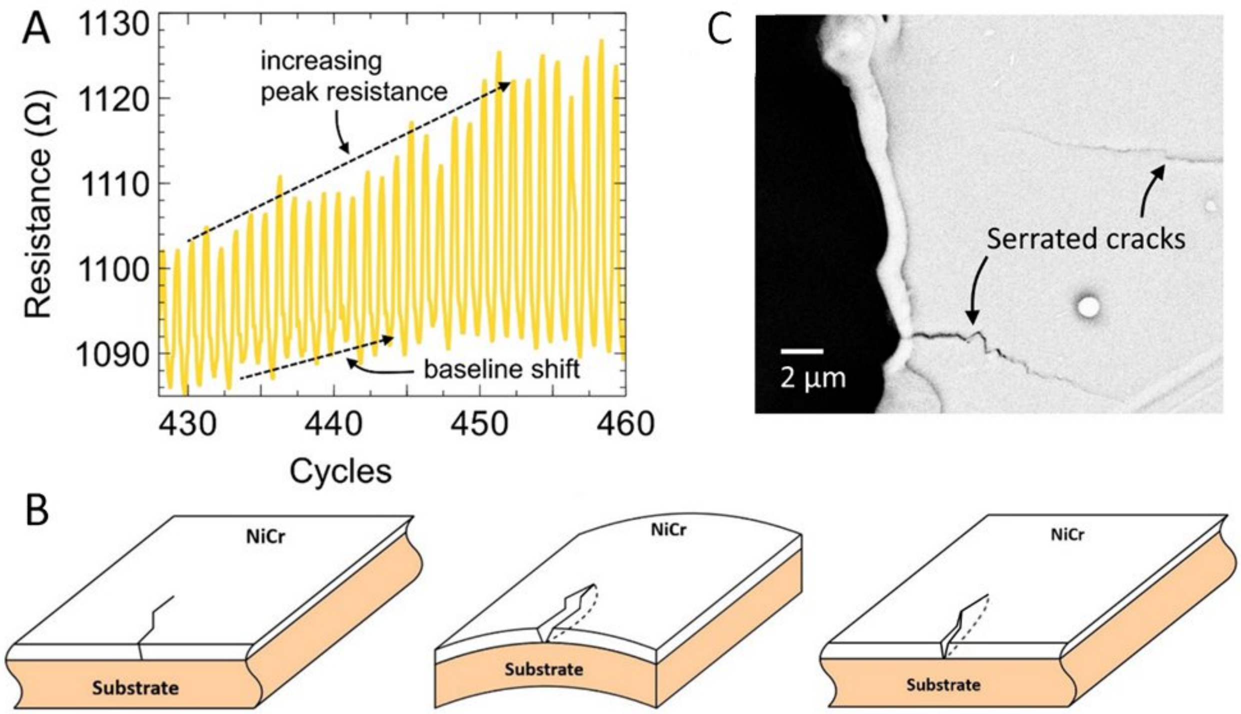

Figure 10. a) Resistance response showing upward shift in baseline with increasing peak resistance; b) schematics showing a crack from initial unstrained condition, crack opening during bending, and crack remaining partially open after stress release; c) SEM image of a crack in the unstrained position.

All cracks observed in the Evanohm traces initiated from the edge and propagated across the trace. Several possible approaches can be used to address this. The first is to reduce edge defects that appear during manufacturing, which may act as initial sites for crack formation during loading. These defects are theorized to occur due to thermal cycling during patterning and molten material solidifying after laser exposure. This can be addressed by using picosecond or femtosecond laser systems that rely less on the photothermal effect to remove material. Otherwise, reducing the pulse energy and increasing the number of passes by the UV nanosecond laser to minimize the thermal gradients and the quantity of molten material generated during processing can also address the formation of these defects. Secondly, the serrated nature of the trace edges may introduce regions with higher stress concentration during bending, encouraging crack nucleation and propagation. Careful control of pulse overlap can be used to obtain straighter edges. Lastly, applying a suitable coating with sufficient stiffness [27] could deter manufacturing defects from propagating or fatigue cracks from forming, although care would have to be taken to prevent the coating from affecting the sensitivity of the strain gauge.

4. Conclusions

The laser fabrication of a flexible thin-film strain gauge using UV laser ablation was demonstrated. The strain gauge characteristics and the dynamic tensile performance were evaluated:

- The experimentally measured resistance for the fabricated strain gauges (1048 Ω ±53 Ω) was close to the expected theoretical resistance of 1025 Ω. Additionally, a gauge factor of 2.3 ±0.2 was measured, which matches the gauge factor of commercially available Evanohm foil-based strain gauges.
- Resistance measurements of individual strain gauge traces after cyclic loading in both the strained and unstrained conditions exhibited that failure was attributed to defects occurring on a fraction of traces while the majority continued to function normally.
- Fatigue failure (< 10^6 cycles) during cyclic tensile loading was not observed below 1750 με, and the highest strain level at which a strain gauge experienced runout was 2625 με.
- Several failure mechanisms were identified. Open circuit failures in samples that survived 10^3 to 10^5 cycles were attributed to the growth of fatigue crack networks in the sensing layer. Response degradation of samples that survived less than 10^3 cycles were attributed to two types of failures. The first is a combination of cracking and delamination, which manifested as a peak in the unstrained resistance during cyclic testing. The second is the growth of cracks without delamination which manifested as an increasing baseline resistance and an increasing peak resistance.

Acknowledgements

This work was supported with funding from the Natural Sciences and Engineering Research Council of Canada (NSERC), the Canada Research Chairs (CRC) Program, and Forcen Inc., and was performed at the University of Waterloo's Centre for Advanced Materials Joining.

References

[1] Choi H, Choi S, Cha H. Structural Health Monitoring system based on strain gauge enabled wireless sensor nodes. Proceedings of INSS 2008 - 5th International Conference on Networked Sensing Systems 2008:211–4. https://doi.org/10.1109/INSS.2008.4610888.

[2] Cheng M, Zhu G, Zhang F, Tang W lai, Jianping S, Yang J quan, et al. A review of flexible force sensors for human health monitoring. Journal of Advanced Research 2020;26:53–68. https://doi.org/10.1016/J.JARE.2020.07.001.

[3] Leal-Junior AG, Frizera A, Marques C, Sánchez MRA, Botelho TR, Segatto M v., et al. Polymer optical fiber strain gauge for human-robot interaction forces assessment on an active knee orthosis. Optical Fiber Technology 2018;41:205–11. https://doi.org/10.1016/J.YOFTE.2018.02.001.

[4] Bethe K, Schön D. Thin-film strain-gauge transducers. vol. 39. 1980.

[5] Lichtenwalner DJ, Hydrick AE, Kingon AI. Flexible thin film temperature and strain sensor array utilizing a novel sensing concept. Sensors and Actuators A: Physical 2007;135:593–7. https://doi.org/10.1016/J.SNA.2006.07.019.

[6] Bose AK, Zhang X, Maddipatla D, Masihi S, Panahi M, Narakathu BB, et al. Screen-printed strain gauge for micro-strain detection applications. IEEE Sensors Journal 2020;20:12652–60. https://doi.org/10.1109/JSEN.2020.3002388.

[7] Lind JU, Yadid M, Perkins I, O'Connor BB, Eweje F, Chantre CO, et al. Cardiac microphysiological devices with flexible thin-film sensors for higher-throughput drug screening. Lab on a Chip 2017;17:3692–703. https://doi.org/10.1039/C7LC00740J.

[8] Lee J, Cho D, Chen H, Shim Y-S, Park J, Jeon S. Proximity-field nanopatterning for high-performance chemical and mechanical sensor applications based on 3D nanostructures. Applied Physics Reviews 2022;9:011322. https://doi.org/10.1063/5.0081197.

[9] Nam SH, Hyun G, Cho D, Han S, Bae G, Chen H, et al. Fundamental principles and development of proximity-field nanopatterning toward advanced 3D nanofabrication. Nano Research 2021 14:9 2021;14:2965–80. https://doi.org/10.1007/S12274-021-3428-6.

[10] Longtin J, Sampath S, Tankiewicz S, Gambino RJ, Greenlaw RJ. Sensors for Harsh Environments by Direct-Write Thermal Spray. IEEE Sensors Journal 2004;4:118–21. https://doi.org/10.1109/JSEN.2003.822218.

[11] Overmeyer L, Duesing JF, Suttmann O, Stute U. Laser patterning of thin film sensors on 3-D surfaces. CIRP Annals 2012;61:215–8. https://doi.org/10.1016/J.CIRP.2012.03.087.

[12] Suttmann O, Gosselin M, Klug U, Kling R. Picosecond laser patterning of NiCr thin film strain gages. Frontiers in Ultrafast Optics: Biomedical, Scientific, and Industrial Applications X 2010;7589:758914. https://doi.org/10.1117/12.840842.

[13] Li L, Hong M, Schmidt M, Zhong M, Malshe A, Huis In'Tveld B, et al. Laser nano-manufacturing – State of the art and challenges. CIRP Annals 2011;60:735–55. https://doi.org/10.1016/J.CIRP.2011.05.005.

[14] Warkusz F. Electrical and mechanical properties of thin metal films: Size effects. Progress in Surface Science 1980;10:287–382. https://doi.org/10.1016/0079-6816(80)90003-9.

[15] Aguilar CA, Lu Y, Mao S, Chen S. Direct micro-patterning of biodegradable polymers using ultraviolet and femtosecond lasers. Biomaterials 2005;26:7642–9. https://doi.org/10.1016/J.BIOMATERIALS.2005.04.053.

[16] Wang L, Wang Z, Bakhtiyari AN, Zheng H. A Comparative Study of Laser-Induced Graphene by CO2 Infrared Laser and 355 nm Ultraviolet (UV) Laser. Micromachines 2020, Vol 11, Page 1094 2020;11:1094. https://doi.org/10.3390/MI11121094.

[17] Brown MS, Arnold CB. Fundamentals of Laser-Material Interaction and Application to Multiscale Surface Modification. Laser Precision Microfabrication, vol. 135, 2010, p. 91–120. https://doi.org/10.1007/978-3-642-10523-4.

[18] Besner S, Meunier M. Laser Synthesis of Nanomaterials. In: Sugioka K, Meunier M, Piqué A, editors. vol. 135, Berlin, Heidelberg: Springer Berlin Heidelberg; 2010, p. 163–87. https://doi.org/10.1007/978-3-642-10523-4_7.

[19] Hewlett-Packard Co. Practical Strain Gage Measurements. Application Note 290-1. Palo Alto, California: Hewlett-Packard Co.; 1981.

[20] Witt GR. The electromechanical properties of thin films and the thin film strain gauge. Thin Solid Films 1974;22:133–56. https://doi.org/10.1016/0040-6090(74)90001-7.

[21] Jung H, Park C, Lee H, Hong S, Kim H, Cho SJ. Nano-Cracked Strain Sensor with High Sensitivity and Linearity by Controlling the Crack Arrangement. Sensors 2019;19:2834. https://doi.org/10.3390/s19122834.

[22] Kazi IH, Wild PM, Moore TN, Sayer M. Characterization of sputtered nichrome (Ni-Cr 80/20 wt.%) films for strain gauge applications. Thin Solid Films 2006;515:2602–6. https://doi.org/10.1016/j.tsf.2005.10.077.

[23] Vishay Precision Group. Fatigue Characteristics of Micro-Measurements Strain Gages. 2010.

[24] Kraft O, Schwaiger R, Wellner P. Fatigue in thin films: Lifetime and damage formation. Materials Science and Engineering A 2001;319–321:919–23. https://doi.org/10.1016/S0921-5093(01)00990-X.

[25] Zhang GP, Volkert CA, Schwaiger R, Wellner P, Arzt E, Kraft O. Length-scale-controlled fatigue mechanisms in thin copper films. Acta Materialia 2006;54:3127–39. https://doi.org/10.1016/j.actamat.2006.03.013.

[26] Kim BJ, Shin HAS, Choi IS, Joo YC. Electrical failure and damage analysis of multi-layer metal films on flexible substrate during cyclic bending deformation. Proceedings of the International Symposium on the Physical and Failure Analysis of Integrated Circuits, IPFA 2011. https://doi.org/10.1109/IPFA.2011.5992725.

[27] Luo XM, Zhang B, Zhang GP. Fatigue of metals at nanoscale: Metal thin films and conductive interconnects for flexible device application. Nano Materials Science 2019;1:198–207. https://doi.org/10.1016/J.NANOMS.2019.02.003.